

Experimental Bond Critical Point and Local Energy Density Properties Determined for Mn–O, Fe–O, and Co–O Bonded Interactions for Tephroite, Mn₂SiO₄, Fayalite, Fe₂SiO₄, and Co₂SiO₄ Olivine and Selected Organic Metal Complexes: Comparison with Properties Calculated for Non-Transition and Transition Metal M–O Bonded Interactions for Silicates and Oxides

G. V. Gibbs,[†] R. T. Downs,[‡] D. F. Cox,[§] K. M. Rosso,[#] N. L. Ross,[†] A. Kirfel,[⊥] T. Lippmann,^{||} W. Morgenroth,[∇] and T. D. Crawford[○]

Departments of Geosciences, Chemical Engineering, and Chemistry, Virginia Tech, Blacksburg, Virginia 24061; Department of Geosciences, University of Arizona, Tucson, Arizona 85721; Chemical and Materials Sciences Division and the W. R. Wiley Environmental Molecular Sciences Laboratory, Pacific Northwest National Laboratory, Richland, Washington 99352; Mineralogisch-Petrologisches Institut, Universität Bonn, Poppelsdorfer Schloss, D-53115 Bonn, Germany; GKSS, Max-Planck-Strasse, D-21502 Geesthacht, Germany; and HASYLAB/DESY, Notkestrasse 85, D-22603 Hamburg, Germany

Received: May 14, 2008; Revised Manuscript Received: July 2, 2008

Bond critical point (bcp) and local energy density properties for the electron density (ED) distributions, calculated with first-principle quantum mechanical methods for divalent transition metal Mn-, Co-, and Fe-containing silicates and oxides are compared with experimental model ED properties for tephroite, Mn₂SiO₄, fayalite, Fe₂SiO₄, and Co₂SiO₄ olivine, each determined with high-energy synchrotron single-crystal X-ray diffraction data. Trends between the experimental bond lengths, $R(\text{M}-\text{O})$, ($\text{M} = \text{Mn}, \text{Fe}, \text{Co}$), and the calculated bcp properties are comparable with those observed for non-transition M–O bonded interactions. The bcp properties, local total energy density, $H(\mathbf{r}_c)$, and bond length trends determined for the Mn–O, Co–O, and Fe–O interactions are also comparable. A comparison is also made with model experimental bcp properties determined for several Mn–O, Fe–O, and Co–O bonded interactions for selected organometallic complexes and several oxides. Despite the complexities of the structures of the organometallic complexes, the agreement between the calculated and model experimental bcp properties is fair to good in several cases. The $G(\mathbf{r}_c)/\rho(\mathbf{r}_c)$ versus $R(\text{M}-\text{O})$ trends established for non-transition metal M–O bonded interactions hold for the transition metal M–O bonded interactions with $G(\mathbf{r}_c)/\rho(\mathbf{r}_c)$ increasing in value as $H(\mathbf{r}_c)$ becomes progressively more negative in value, indicating an increasing shared character of the interaction as $G(\mathbf{r}_c)/\rho(\mathbf{r}_c)$ increases in value. As observed for the non-transition metal M–O bonded interactions, the Laplacian, $\nabla^2\rho(\mathbf{r}_c)$, increases in value as $\rho(\mathbf{r}_c)$ increases and as $H(\mathbf{r}_c)$ decreases and becomes progressively more negative in value. The Mn–O, Fe–O, and Co–O bonded interactions are indicated to be of intermediate character with a substantial component of closed-shell character compared with Fe–S and Ni–S bonded interactions, which show greater shared character based on the $|V(\mathbf{r}_c)|/G(\mathbf{r}_c)$ bond character indicator. The atomic charges conferred on the transition metal atoms for the three olivines decrease with increasing atomic number from Mn to Fe to Co as the average M–O bond lengths decrease from 2.219 to 2.168 to 2.128 Å, respectively.

Introduction

Contemporary quantum chemistry presents a quandary. Solution of the Schrodinger equation proceeds to higher and higher accuracy, and molecular properties are computed ever more precisely. But the understanding of molecular properties seems thereby not enhanced. The beauty that is chemistry eludes us. — Robert G. Parr.

The chemical bond is a fundamental concept in chemistry that has provided an important basis for rationalizing the structure, properties, stability, reactivity, and stoichiometry for

a host of materials. Interest in the bond is evinced by the wealth of papers and reviews that have been published on the concept where at times, particularly in textbooks, it has been discussed as if it were a fairly well-understood and simple concept. However, the famous quote by the Nobel Prize winning chemist Robert S. Mulliken, “I believe the chemical bond is not as simple as some people seem to think”, belies the notion that the concept is well-understood and simple. As the chemical bond is not a quantum mechanical construct, Coulson¹ has asserted that “a chemical bond is not a real thing: it does not exist: no one has ever seen it, no one ever can. It is a figment of our own imagination.” In a description of bonded interactions in terms of the local properties of the electron density, Cremer and Kraka² stated that “There is no way to measure a bond nor any of its properties.” Bader³ added further that “There are no chemical bonds, just bonded atoms.” In contrast, Linus Pauling,⁴ a strong advocate for the existence of the chemical bond, has written in

[†] Department of Geosciences, Virginia Tech.

[‡] University of Arizona.

[§] Departments of Chemical Engineering, Virginia Tech.

[#] Pacific Northwest National Laboratory.

[⊥] Universität Bonn.

^{||} GKSS.

[∇] HASYLAB/DESY.

[○] Departments of Chemistry, Virginia Tech.

his famous book, *The Nature of the Chemical Bond*, that quantum mechanics has not only dispersed the veil of mystery that has shrouded the chemical bond, but that it has also introduced into chemical theory the concept of resonance, the electron pair bond, hybridization, and a set of formal rules for the formation of covalent bonds. However, as countered by Coulson,⁵ "Concepts like hybridization, resonance, covalent and ionic structures do not appear to correspond to anything directly measurable."

Upon concluding that a chemical bond can be neither defined nor measured, Bader and his colleagues⁶ undertook the challenge of searching for a feature in the electron density (ED) distribution that might qualify as a representative of a bonded interaction. Unlike a chemical bond, the ED distribution is the measurable expectation value of the density operator, a quantum mechanical observable. Furthermore, the ED is a robust property that embodies all of the information that can be known about a ground-state material, including its kinetic, potential, and total energy.⁷ In the exploration for evidence of a bonded interaction, the ED distributions for a variety of molecules were surveyed in a search for features that matched their perception as to what a bonded interaction might look like. The one feature that caught their attention and resembled what was perceived as having the defining characteristics of a bonded interaction was a path of ED that connects the nuclei of adjacent atoms. Their study revealed that in fact the path consists of a pair of paths of steepest ascent in the gradient field of the ED, both of which originate at a point on the path between the pair of atoms where $\nabla\rho(\mathbf{r}) = 0$. One path terminates at the nucleus of one of the atoms, and the other terminates at the nucleus of the other. Combined, the two paths were established to consist of a continuous pathway of maximum ED, relative to any neighboring pathway. Bader⁸ and later Runtz et al.⁹ defined the pathway as the bond path and the local minimum along the path as the bond critical point, \mathbf{r}_c . Furthermore, the value of the ED at \mathbf{r}_c , denoted $\rho(\mathbf{r}_c)$, was found to increase as a given bond length decreases and the strength of the bonded interaction increases. It was also asserted that the existence of the bond path and its bond critical point are necessary and sufficient conditions for the pair to be bonded in the chemical sense.¹⁰ As the path is also mirrored by a line of maximally stabilizing potential energy density that links the nuclei, it was concluded that the bond path is a universal indicator of a bonded interaction, linking all pairs of bonded atoms, regardless of the nature of the interaction.¹¹ Despite the connection between a bond path and a bonded interaction, Bader⁶ was careful to stress that a bond path represents a bonded interaction, not a chemical bond.

Properties of the Electron Density at the Bond Critical Point. The properties of a bonded interaction, defined by the distribution of the ED along the bond path in the immediate vicinity of \mathbf{r}_c , were found by evaluating the ED at \mathbf{r}_c and at the corners, the centers of the edges, and faces of a tiny cube ($\sim 10^{-6}$ au on an edge) centered at \mathbf{r}_c and fitting the measured $\rho(\mathbf{r})$ values to the second-order Taylor series expansion⁶

$$\rho(\mathbf{r}) = \rho(\mathbf{r}_c) + (\mathbf{r} - \mathbf{r}_c)^T \nabla \rho(\mathbf{r}_c) + \frac{1}{2} (\mathbf{r} - \mathbf{r}_c)^T H_{ij} (\mathbf{r} - \mathbf{r}_c) \quad (1)$$

where $\nabla\rho(\mathbf{r}_c) = 0$ and $H_{ij} = \partial^2\rho(\mathbf{r}_c)/\partial x_i \partial x_j$, $i, j = (1, 3)$. As H_{ij} is a symmetrical matrix, it can be diagonalized where the diagonal elements of the matrix, Λ , define the curvatures of $\rho(\mathbf{r}_c)$ with respect to each of the associated eigenvectors \mathbf{e}_i , $i = 1, 3$. The trace of the matrix $\text{tr}(\Lambda) = \lambda_1 + \lambda_2 + \lambda_3$, where $\lambda_1 = \partial^2\rho(\mathbf{r}_c)/\partial x_1^2$, $\lambda_2 = \partial^2\rho(\mathbf{r}_c)/\partial x_2^2$, and $\lambda_3 = \partial^2\rho(\mathbf{r}_c)/\partial x_3^2$ such that $\text{tr}(\Lambda) = \partial^2\rho(\mathbf{r}_c)/\partial x_1^2 + \partial^2\rho(\mathbf{r}_c)/\partial x_2^2 + \partial^2\rho(\mathbf{r}_c)/\partial x_3^2$ is the divergence of the gradient of $\rho(\mathbf{r}_c)$ defined as the Laplacian of

$\rho(\mathbf{r}_c)$, $\nabla^2\rho(\mathbf{r}_c)$. The two curvatures of the ED distribution, $\lambda_1 = \partial^2\rho(\mathbf{r}_c)/\partial x_1^2$ and $\lambda_2 = \partial^2\rho(\mathbf{r}_c)/\partial x_2^2$, associated with the eigenvectors \mathbf{e}_1 and \mathbf{e}_2 , respectively, are both negative and measure the extent to which the ED is locally concentrated perpendicular to the bond path at \mathbf{r}_c , and the third, $\lambda_3 = \partial^2\rho(\mathbf{r}_c)/\partial x_3^2$, associated with the third eigenvector \mathbf{e}_3 , is positive and measures the extent to which the ED is locally depleted at \mathbf{r}_c and locally concentrated in the basins of the atoms, thereby shielding the bonded atoms. The distances between the nuclei of a pair of bonded atoms M and O and \mathbf{r}_c , respectively, are defined as the bonded radius of M, denoted $r_b(M)$, and the bonded radius of O, denoted $r_b(O)$, respectively. The three curvatures λ_1 , λ_2 , and λ_3 , the values of $\rho(\mathbf{r}_c)$ and $\nabla^2\rho(\mathbf{r}_c)$, and the bonded radii (all observables) are collectively referred to as the bond critical point properties of a bonded interaction.

Previous Studies. The ED distributions, bcp properties, and local energy density properties have been calculated for a relatively large number of silicates and oxides containing first- and second-row non-transition metal M atoms bonded to O.^{12,13} The calculations were completed, using the observed cell dimensions, the space group type, and the coordinates of the atoms with CRYSTAL98 and Bloch functions expanded as linear combinations of atomic centered Gaussian-type basis sets.¹⁴ Self-consistent field wave functions, solved in reciprocal space, were computed for each structure at the density functional theory level using the local density approximation formulated with the Vosko–Wilk–Nusair parametrization of the correlation potential. The basis sets used in the calculations were specifically optimized for the CRYSTAL98 program.¹⁴ The bcp and the local energy density properties were generated from the ED distributions with TOPOND software.¹⁵

The values of $\rho(\mathbf{r}_c)$ and $\nabla^2\rho(\mathbf{r}_c)$ generated in the calculations were found to increase nonlinearly for each bonded interaction as the experimental M–O bond lengths, $R(M-O)$ ($M = \text{Be}, \dots, \text{C}; \text{Na}, \dots, \text{S}$) decrease.^{12,13} The negative curvatures λ_1 and λ_2 evaluated at \mathbf{r}_c were likewise observed to decrease further in value as $R(M-O)$ decreases, establishing that the ED is progressively locally concentrated perpendicular to the bond paths at \mathbf{r}_c as the bond lengths shorten and as $\rho(\mathbf{r}_c)$ increases in value. Concomitant with the decrease in the values of λ_1 and λ_2 , the values of λ_3 were observed to increase, demonstrating that the ED is progressively locally depleted at \mathbf{r}_c and locally concentrated in the direction of the M and O atoms as the bond lengths shorten, resulting in a local charge concentration in the basins of the bonded atoms. The values of $\nabla^2\rho(\mathbf{r}_c)$ for the M–O bonded interactions are each positive, except for several of the C–O bonded interactions, each of which was observed to increase roughly along parallel trends when plotted with respect to $\rho(\mathbf{r}_c)$. As observed by Gatti,¹⁶ the ED adopted at equilibrium is the best compromise that yields the lowest energy for the system as a whole. As such, the ED accumulated along the bond paths is considered to locally stabilize a bonded interaction relative to the pair of atoms lacking a bond path. As the M–O bond lengths decrease with increasing $\rho(\mathbf{r}_c)$ and $\nabla^2\rho(\mathbf{r}_c)$, the nuclei of the bonded atoms are progressively shielded by the progressive accumulation of the ED along the bond path in the internuclear region and the progressive local concentration of the ED toward the bonded atoms, thereby locally stabilizing the system. Furthermore, the competition among the M–O exchange correlation energies always serves to stabilize an M–O bonded interaction.¹⁷ Given the nonlinear relationships between $R(M-O)$ and $\rho(\mathbf{r}_c)$ and $\nabla^2\rho(\mathbf{r}_c)$, respectively, the value of $\nabla^2\rho(\mathbf{r}_c)$ increases linearly as the value of $\rho(\mathbf{r}_c)$ increases. The greater the accumulation of ED for a given bonded interaction,

the larger is the value of the Laplacian, such that for shared interactions the local potential energy density dominates the local kinetic energy at \mathbf{r}_c (see below).

Since the Downs and Swope¹⁸ pioneering study of the ED distribution for the borosilicate danburite, $\text{CaB}_2\text{Si}_2\text{O}_8$, model experimental ED density distributions and bcp properties have been determined for several other minerals. In the modeling of an experimental ED distribution, the ED associated with each nonequivalent atom is represented by a spherical core and a valence shell of ED that is unconstrained and that can expand or contract, depending on the atomic charge and the deformation of the ED of the valence shell. Simply stated, the spherical core and the deformed valence ED for each atom, i , is represented by a multipole expansion $P_{ilm}R_i(\mathbf{r})Y_{lm}(\theta,\phi)$, where P_{ilm} is a population parameter, $R_i(\mathbf{r})$ is a radial distribution Slater type function or a linear combination of exponentials, and $Y_{lm}(\theta,\phi)$ is an appropriate set of spherical tesseral harmonics.¹⁹ The software VALRAY,²⁰ for example, applies the nuclei centered, flexible pseudoatom multipole expansions of the ED to each nonequivalent atom defined in terms of one common Cartesian basis set used in modeling the total ED distribution for the crystal. The experimental population parameters P_{ilm} are then determined in a least-squares refinement in terms of the observed X-ray structure amplitudes. Upon completion of the multipole refinement, the resulting model multipole representation of the ED distribution is subjected to a topological analysis in the determination of the experimental model bcp properties for the bonded interactions in the crystal.

For ED model distributions determined with conventional single-crystal X-ray diffraction data, the agreement between the model experimental and calculated properties for the bonded M–O interactions has been found to range between poor and in some cases even moderately good.²¹ For example, the model experimental $\rho(\mathbf{r}_c)$ values obtained for the B–O and Si–O bonded interactions for danburite¹⁸ and the Si–O bonded interactions in coesite,²² a high-pressure polymorph of SiO_2 , are in fair to moderately good agreement with the calculated values, whereas the agreement for the Al–O and Si–O bonded interactions for the fibrous zeolites²³ is poor. The experimental $\rho(\mathbf{r}_c)$ values depart by as much as 30% from the calculated values and fail to show a trend with the experimental bond lengths. The experimental $\rho(\mathbf{r}_c)$ values for the Si–O bonded interactions for both danburite and coesite also show little correlation with bond length as predicted by the calculations, whereas the experimental values for the B–O bonded interactions roughly parallel the calculated trend. The model experimental $\nabla^2\rho(\mathbf{r}_c)$ values for danburite and coesite are in poorer agreement with the calculated values [as may be expected given that $\nabla^2\rho(\mathbf{r}_c)$ is the second derivative of $\rho(\mathbf{r}_c)$], whereas the experimental values for the zeolites show even greater departures from the calculated values, by as much as several hundred percent. However, the experimental $\rho(\mathbf{r}_c)$ and $\nabla^2\rho(\mathbf{r}_c)$ values for the Na–O and Ca–O bonded interactions for danburite and the fibrous zeolites tend to cluster along the calculated trends established between the experimental bond lengths and the calculated values for $\rho(\mathbf{r}_c)$ and $\nabla^2\rho(\mathbf{r}_c)$, respectively. In contrast with the previous results, the experimental $\rho(\mathbf{r}_c)$ and $\nabla^2\rho(\mathbf{r}_c)$ values determined for the Sb_2O_3 polymorphs senarmonite and valentinite²⁴ and more recently for coesite²⁵ using high-resolution single-crystal X-ray diffraction data and that determined for cuprite, CuO_2 ,²⁶ and stishovite, a very high pressure polymorph of SiO_2 ,²⁷ using high-energy synchrotron single-crystal data (that are largely free of absorption, extinction, and multiple scattering) are comparable and often in better agreement

with the calculated values.²¹ Given the improved agreement of the high-resolution and particularly the synchrotron diffraction data sets, as compared with conventional data sets,²⁸ the comparability of the experimental and calculated bcp properties for such data sets is considered to be adequate.²⁹ Of course, inasmuch as the curvatures and the Laplacian of the ED involve second derivatives, the experimental values obtained with the more accurate experimental methods may also still show poorer agreement with the calculated values than the $\rho(\mathbf{r}_c)$ values.

In addition to the data sets collected for coesite and stishovite, high-resolution single-crystal diffraction data have also been determined for the silicates scolecite, $\text{CaAl}_2\text{Si}_3\text{O}_{10}\cdot 3\text{H}_2\text{O}$,³⁰ and diopside, $\text{CaMgSi}_2\text{O}_6$,³¹ together with high-energy synchrotron data for forsterite, Mg_2SiO_4 ,³² fayalite,³³ tephroite,³⁴ and Co_2SiO_4 .³⁵ For each case, the model experimental bcp properties were obtained by aspherical multipole modeling of the experimental ED distributions. The experimental model bcp properties obtained for the Si–O interactions for these minerals are comparable with those calculated.^{13,21} The agreement between the experimental $\rho(\mathbf{r}_c)$ values for stishovite, coesite, scolecite, and diopside and the calculated values is considered to be fairly good to good. It is noteworthy, however, that the $\rho(\mathbf{r}_c)$ values for the Si–O bonded interactions for four olivines systematically exceed the calculated trend by $\sim 10\%$ ¹³ and roughly parallel the calculated values. The experimental $\lambda_{12} = \frac{1}{2}|\lambda_1 + \lambda_2|$ values for the minerals are also considered to be in fairly good agreement with the calculated values, whereas the experimental λ_3 and $\nabla^2\rho(\mathbf{r}_c)$ values for scolecite and the olivines are smaller than the calculated trends by as much as $\sim 30\%$ in several cases, a result that is again not entirely unexpected given that these properties are second derivatives of $\rho(\mathbf{r}_c)$. Furthermore, a critical examination of the radial functions used in the experimental multipole modeling of the ED has revealed that it fails to correctly model λ_3 , the curvature of the ED along the bond path.³⁶ As a result, the overall error in the experimental value of $\nabla^2\rho(\mathbf{r}_c)$ can be as much as 50%,³⁷ particularly in the case of shared interactions. Nonetheless, the trends defined by $R(\text{Si–O})$ versus λ_3 and $\nabla^2\rho(\mathbf{r}_c)$ roughly parallel the calculated trends. Overall, the experimental results recorded for the two silica polymorphs coesite²⁵ and stishovite,²⁷ which contain only Si and O, show the most satisfactory overall agreement with the calculated values and fall largely within the scatter of the calculated bcp data.¹³ The use of Hirshfeld³⁸ type radial functions in the modeling of the experimental ED for coesite may account in part for the agreement of the experimental and calculated λ_3 and $\nabla^2\rho(\mathbf{r}_c)$ values reported for the silica polymorph.²⁵ The use of the radial functions also resulted in a substantial improvement in the model static deformation maps together with the removal of a spurious ring of ED $\sim 0.25 \text{ e}/\text{\AA}^3$ in height that was observed to surround each Si atom in coesite generated in the refinement with a single exponential radial function.

The model experimental bcp properties determined with synchrotron and high-resolution single-crystal diffraction data for the Mg–O bonded interactions recorded for forsterite³² and diopside,³¹ respectively, are compared with those calculated for the Mg–O bonded interactions for a number of Mg–O-bearing silicates and oxides (Figure 1). The experimental model properties for the interactions reported for forsterite are comparable with those calculated and scatter within or close to the scatter of the calculated data. In the case for diopside, only the values for $\rho(\mathbf{r}_c)$ and $\nabla^2\rho(\mathbf{r}_c)$ were reported.³¹ These values are likewise comparable with those calculated, with one point falling outside the scatter of the calculated data set. It is noteworthy that the

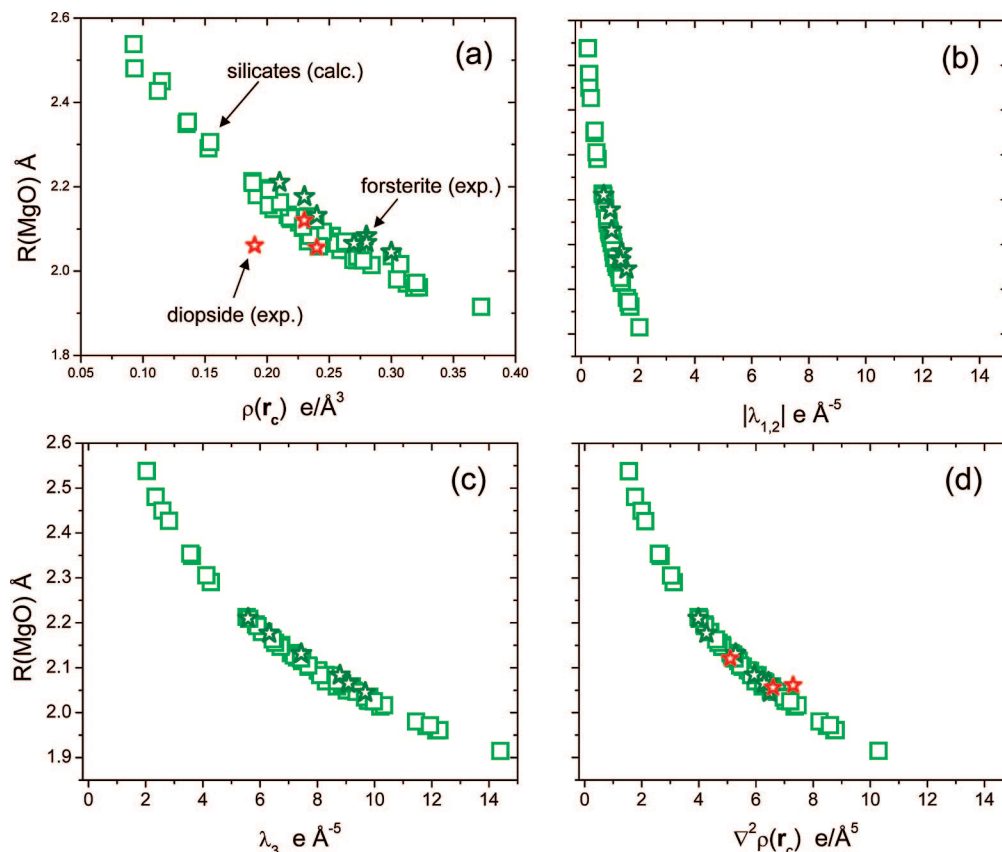


Figure 1. Experimental Mg–O bond lengths, $R(\text{Mg–O})$ Å plotted with respect to the bcp properties (a) $\rho(\mathbf{r}_c)$, (b) $|\lambda_{1,2}| = 1/2|\lambda_1 + \lambda_2|$, (c) λ_3 , and (d) $\nabla^2\rho(\mathbf{r}_c)$ calculated for Mg–O-bearing silicates and oxides (green squares). Model experimental Mg–O bcp properties determined for diopside (red stars)³¹ and forsterite (green stars)³² are added to the figure for comparison.

experimental bcp properties reported for the Ca–O bonded interactions involving the nominally divalent Ca cations of scolecite³⁰ are also in moderately good agreement with those calculated.²¹ By and large, like the agreement between the experimental and theoretical properties for the Si–O bonded interactions, the agreement for the Mg–O interactions in forsterite and the Ca–O and Na–O interactions in the fibrous zeolites scolecite and in danburite can be considered to be adequate as prescribed by the criteria set forth by Koritsansky and Coppens.²⁹ It is noteworthy that the agreement between the experimental and calculated bcp properties is often better for the more closed shell interactions of a structure than it is for the more shared ones.

Local Energy Density Properties. In addition to the bond critical point properties, the calculated ED distributions provide important information about the local energy density properties for the bonded interactions. As observed by Bader,⁶ the positive definite kinetic energy, $G(\mathbf{r}_c)$, can be directly related to the inner product of the gradients of the orbital electron densities ρ_i and their occupation numbers, n_i , by the expression

$$G(\mathbf{r}) = \frac{1}{8} \sum_i n_i [\nabla\rho_i(\mathbf{r}) \cdot \nabla\rho_i(\mathbf{r}) / \rho_i(\mathbf{r})] \quad (2)$$

where the summation is carried out over the occupied natural spin–orbital components. With the determination of $G(\mathbf{r})$, the negative definite local potential energy density, $V(\mathbf{r})$, can be determined with the local form of the virial theorem $V(\mathbf{r}) = 1/4\nabla^2\rho(\mathbf{r}) - 2G(\mathbf{r})$.⁶ However, the experimental determination of $G(\mathbf{r})$ and $V(\mathbf{r})$ requires approximations based on corrected electron gas theory (see below).³⁹ For shared interactions, the value of $G(\mathbf{r}_c)$ and the magnitude of $V(\mathbf{r}_c)$ have been observed to increase in value for the M–O non-transition metal bonded

interactions as $R(\text{M–O})$ decreases and $\rho(\mathbf{r}_c)$ increases in value⁴⁰ (Figure 2a). As the local total energy density⁶ $H(\mathbf{r}_c) = G(\mathbf{r}_c) + V(\mathbf{r}_c)$ becomes progressively more negative, $\nabla^2\rho(\mathbf{r}_c)$ is observed to become progressively more positive in value as $\rho(\mathbf{r}_c)$ increases. This result is at odds with the assertion that $\nabla^2\rho(\mathbf{r}_c)$ should decrease and become negative as $H(\mathbf{r}_c)$ becomes progressively more negative for shared bonded interactions. As the Laplacian does not suffice to detect all shared bonded interactions, Cremer and Kraka² have asserted that it would be more appropriate to choose $H(\mathbf{r}_c)$ as an indicator of a bonded interaction in place of $\nabla^2\rho(\mathbf{r}_c)$.

Accordingly, $H(\mathbf{r}_c)$ has been used by Cremer and Kraka² to classify bonded interactions. When $V(\mathbf{r}_c) < 0$ and $|V(\mathbf{r}_c)| > G(\mathbf{r}_c)$ such that $H(\mathbf{r}_c)$ is necessarily negative, a bonded interaction is defined as a shared interaction, whereas when $|V(\mathbf{r}_c)| < G(\mathbf{r}_c)$, it is defined as a closed-shell interaction. Unlike $\nabla^2\rho(\mathbf{r}_c)$, the sign of which is determined by $G(\mathbf{r}_c) + V(\mathbf{r}_c)$, the sign of $H(\mathbf{r}_c)$ is determined by the ED itself, and according to Bone and Bader,⁴¹ it is negative, $|V(\mathbf{r}_c)| > G(\mathbf{r}_c)$, for all interactions that result in an accumulation of ED at \mathbf{r}_c .

With decreasing M–O bond length, the value of $V(\mathbf{r}_c)$ is observed to decrease linearly as λ_1 and λ_2 both decrease as the ED is locally concentrated perpendicular to the bond path, whereas the value of $G(\mathbf{r}_c)$ increases linearly as λ_3 increases as the ED is locally depleted at the bcp in the direction of the bonded atoms and concentrated in the basins of the bonded atoms as observed for the Be–O, B–O, C–O, Al–O, Si–O, P–O, S–O bonded interactions. As $H(\mathbf{r}_c)$ is negative for each interaction, each qualifies as a shared interaction.² In contrast, the magnitude of the local energy density, $|V(\mathbf{r}_c)|$, is observed to be less than $G(\mathbf{r}_c)$ for the Na–O and Mg–O interactions

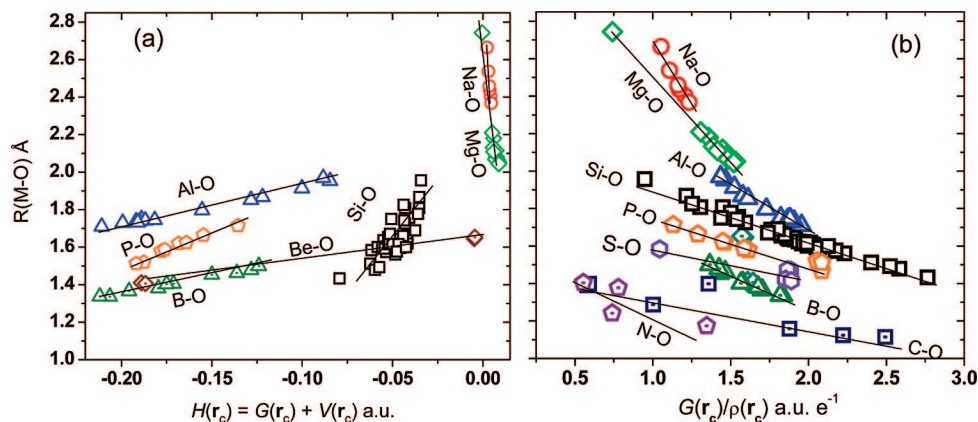


Figure 2. Experimental M–O bond length, $R(\text{M–O})$, for M–O bonded interactions for selected first- and second-row metal atoms M bonded to oxygen plotted (a) with respect to the local total energy density $H(\mathbf{r}_c) = G(\mathbf{r}_c) + V(\mathbf{r}_c)$ au, where $G(\mathbf{r}_c)$ is the local kinetic energy density and $V(\mathbf{r}_c)$ is the local potential energy density⁶ (note that the slopes for the Mg–O and Na–O bonded interactions are negative) and (b) with respect to the $G(\mathbf{r}_c)/\rho(\mathbf{r}_c)$ ratio au e^{-1} .

such that $H(\mathbf{r}_c)$ is positive and each of the interactions qualifies as a closed-shell interaction (Figure 2a).⁴⁰ As observed above for the shared interactions, ED accumulates progressively at \mathbf{r}_c as $H(\mathbf{r}_c)$ becomes progressively more negative in value. However, it actually accumulates at \mathbf{r}_c when $H(\mathbf{r}_c)$ is positive and increases slightly in value as evinced by the decrease in the bond length and the progressive increase in $\rho(\mathbf{r}_c)$ observed for the Li–O, Na–O, and Mg–O interactions (Figure 2a).

It is generally accepted that the ratio $G(\mathbf{r}_c)/\rho(\mathbf{r}_c)$ is less than unity for shared interactions and greater for closed-shell interactions.^{6,16,42–45} Yet, for the non-transition metal M–O bonded interactions studied by Gibbs et al.,⁴⁰ the converse was found to hold with the $G(\mathbf{r}_c)/\rho(\mathbf{r}_c)$ ratio exceeding unity in a linear fashion for a given bonded interaction with decreasing bond length (Figure 2b) and, with the exception of the Na–O and Mg–O bonded interactions, with decreasing negative values of $H(\mathbf{r}_c)$ (Figure 2a). As the shared character for a given M–O interaction has been established to increase with decreasing coordination number,^{46–48} the increasing value of $G(\mathbf{r}_c)/\rho(\mathbf{r}_c)$ displayed in the figure with decreasing coordination number and bond length for a given bonded interaction is consistent with the assertion that the $G(\mathbf{r}_c)/\rho(\mathbf{r}_c)$ ratio increases with increasing shared character.⁴⁰ Also, for the shared interactions, the ratio increases as $H(\mathbf{r}_c)$ decreases and becomes progressively more negative in value, whereas for closed-shell interactions (Na–O, Mg–O) the converse holds and $G(\mathbf{r}_c)/\rho(\mathbf{r}_c)$ increases as $H(\mathbf{r}_c)$ increases and becomes progressively more positive (Figure 2a). The ratio $H(\mathbf{r}_c)/\rho(\mathbf{r}_c)$, defined as the bond degree, has been interpreted as the total pressure per electron unit at \mathbf{r}_c ;⁴⁹ the more negative the value of the ratio, the more shared the interaction.

It will be important to establish whether $G(\mathbf{r}_c)/\rho(\mathbf{r}_c)$ increases in value for the transition Mn–O, Fe–O, and Co–O bonded interactions for tephroite, fayalite, and the Co_2SiO_4 olivine, respectively, as the experimental M–O bond lengths decrease in length as observed for the non-transition M–O interactions.⁴⁰ Following a study of a relatively wide variety of different materials including organometallic complexes, Bianchi et al.⁵⁰ has concluded that there is no particular trend that involves the $G(\mathbf{r}_c)/\rho(\mathbf{r}_c)$ ratio for any type of bonded interaction. If true, then the trend reported between $R(\text{M–O})$ and $G(\mathbf{r}_c)/\rho(\mathbf{r}_c)$ for the non-transitional bonded interactions may well be a singular case⁴⁰ and restricted in its application. However, an examination of recent evidence, for example, presented by Gatti and Lasi⁵¹ for the Co–Co bonded interactions comprising several unsaturated

$\text{Co}_2(\text{CO})_x$ ($x = 8–5$) binuclear 3d metal carbonyls shows a trend with the Co–Co bond lengths correlating with the $G(\mathbf{r}_c)/\rho(\mathbf{r}_c)$ ratio, increasing regularly from 0.57 to 1.09 as the Co–Co separations decrease from 2.49 to 2.17 Å, as $H(\mathbf{r}_c)$ decreases from -0.0189 to -0.0270 and as the $|V(\mathbf{r}_c)|/G(\mathbf{r}_c)$ indicator decreases from 1.67 to 1.31, with the shorter Co–Co separations involving larger $G(\mathbf{r}_c)/\rho(\mathbf{r}_c)$ values. Furthermore, an examination of the $G(\mathbf{r}_c)/\rho(\mathbf{r}_c)$ ratios reported for the hydrocarbons $\text{H}_3\text{C–CH}_3$, $\text{H}_2\text{C=CH}_2$, and $\text{HC}\equiv\text{CH}$ likewise shows that the ratio increases regularly from 0.256 to 0.421 to 0.711 au e^{-1} as $R(\text{C–C})$ decreases from 1.531 to 1.340 to 1.210 Å and as $H(\mathbf{r}_c)$ decreases from -0.203 to -0.388 to -0.561 au, respectively.⁴⁴ Although the ratios for the Co–Co and C–C bonded interactions are both less than unity, as expected for shared interactions, the ratio increases systematically in a trend with decreasing bond length as $H(\mathbf{r}_c)$ decreases in value as observed for non-transition M–O bonded interactions. However, in the case of the Co–Co bonded interaction, the $|V(\mathbf{r}_c)|/G(\mathbf{r}_c)$ ratio decreases with decreasing bond length, increasing $G(\mathbf{r}_c)/\rho(\mathbf{r}_c)$, and decreasing $H(\mathbf{r}_c)$, in contradiction with the assertion that $|V(\mathbf{r}_c)|/G(\mathbf{r}_c)$ increases as the shared character of a bonded interaction increases.⁴⁹ Furthermore, Knop et al.⁵² reported for the ground-state $\text{XH} = \text{CH}, \text{NH}, \text{OH},$ and FH molecules, a well-developed trend between $G(\mathbf{r}_c)/\rho(\mathbf{r}_c)$ and the number n of the p electrons in the X atom, the larger the number of p electrons and the shorter the XH bond length, and the larger the value of $G(\mathbf{r}_c)/\rho(\mathbf{r}_c)$.

Transition Metal M–O (M = Mn, Fe, Co) Properties. The properties calculated for the Mn–O, Fe–O, and Co–O bonded interactions for a number of silicates and oxides are compared in this account with the model experimental bcp and the local energy density properties, determined with high-energy synchrotron single-crystal X-ray diffraction data for the three transition metal oxide olivines tephroite, Mn_2SiO_4 ,³⁴ fayalite, Fe_2SiO_4 ,³³ and Co_2SiO_4 ,³⁵ (Table 1). The experimental setup and the data evaluation were the same as those employed in the previous studies completed for stishovite²⁷ and forsterite.³² The quality of the data used is borne out by the final agreement indices, $R(I/F)$, obtained upon completion of the multipole refinements: tephroite, 0.0055; fayalite, 0.0045; and Co-olivine, 0.0074.

The calculated bcp property values are also compared with the experimental model bcp properties determined for (1) the Fe–O bonded interactions comprising three redox active mixed valence trinuclear oxo-centered Fe-centered carboxylates⁵³ and

TABLE 1: Experimental Model Bond Critical Point and Local Density Properties for Tephroite,³⁴ Fayalite,³³ and Co₂SiO₄³⁵ Olivine

bond	$R(\text{M}-\text{O})$ (Å)	$r_b(\text{O})$ (Å)	$\rho(\mathbf{r}_c)$ ($e/\text{Å}^3$)	$\nabla^2(\mathbf{r}_c)$ ($e/\text{Å}^5$)	λ_1 ($e/\text{Å}^5$)	λ_2 ($e/\text{Å}^5$)	λ_3 ($e/\text{Å}^5$)	$G(\mathbf{r}_c)$ (au)	$V(\mathbf{r}_c)$ (au)
Tephroite									
Mn1-O1	2.202	1.122	0.372	5.90	-1.54	-1.48	8.92	0.064	-0.066
Mn1-O2	2.170	1.095	0.420	6.23	-2.00	-1.86	10.08	0.071	-0.078
Mn1-O3	2.253	1.126	0.367	4.95	-1.54	-1.48	7.98	0.057	-0.062
Mn2-O1	2.282	1.154	0.312	4.50	-1.14	-1.11	6.98	0.048	-0.050
Mn2-O2	2.138	1.078	0.430	7.04	-1.95	-1.88	10.88	0.078	-0.083
Mn2-O3	2.157	1.093	0.428	6.36	-1.99	-1.96	10.33	0.073	-0.080
Mn2-O3	2.321	1.175	0.294	4.10	-1.11	-0.94	6.20	0.044	-0.045
Si-O1	1.621	0.961	1.058	15.84	-7.50	-7.37	30.71	0.240	-0.317
Si-O2	1.661	0.992	1.028	13.32	-7.22	-6.75	26.72	0.217	-0.296
Si-O3	1.642	0.983	1.041	16.83	-7.66	-6.85	31.23	0.244	-0.313
Fayalite									
Fe1-O1	2.121	1.079	0.451	6.48	-2.15	-1.93	10.56	0.077	-0.086
Fe1-O2	2.125	1.086	0.434	6.86	-1.96	-1.74	10.56	0.077	-0.083
Fe1-O3	2.237	1.147	0.344	4.69	-1.41	-1.23	7.33	0.053	-0.056
Fe2-O1	2.233	1.140	0.318	4.85	-1.27	-1.16	7.28	0.051	-0.052
Fe2-O2	2.109	1.080	0.444	7.26	-2.08	-1.81	11.14	0.081	-0.087
Fe2-O3	2.063	1.047	0.501	7.84	-2.47	-2.20	12.52	0.092	-0.102
Fe2-O3	2.293	1.180	0.292	3.97	-1.17	-1.06	6.20	0.043	-0.044
Si-O1	1.624	0.952	1.115	16.15	-8.11	-7.73	31.99	0.254	-0.342
Si-O2	1.654	0.972	1.070	13.12	-7.33	-6.88	27.33	0.224	-0.312
Si-O3	1.635	0.959	1.100	14.49	-7.96	-7.39	29.83	0.240	-0.329
Co ₂ SiO ₄									
Co1-O1	2.094	1.050	0.420	6.90	-1.66	-1.57	10.25	0.076	-0.080
Co1-O2	2.091	1.064	0.422	6.84	-1.63	-1.53	10.00	0.075	-0.080
Co1-O3	2.169	1.106	0.371	5.43	-1.36	-1.30	8.08	0.061	-0.064
Co2-O1	2.179	1.106	0.356	5.22	-1.25	-1.24	7.71	0.058	-0.061
Co2-O2	2.073	1.045	0.436	7.22	-1.77	-1.73	10.72	0.080	-0.085
Co2-O3	2.067	1.041	0.445	7.58	-1.90	-1.86	11.28	0.083	-0.088
Co2-O3	2.223	1.135	0.338	4.67	-1.14	-1.04	6.84	0.052	-0.055
Si-O1	1.619	0.941	1.056	15.50	-7.84	-7.47	30.82	0.238	-0.315
Si-O2	1.653	0.965	1.000	11.89	-7.29	-6.75	25.93	0.201	-0.279
Si-O3	1.638	0.956	1.040	14.61	-7.30	-6.83	28.74	0.228	-0.305

an oxidized trinuclear iron complex,⁵³ (2) the Mn-O bonded interactions for two magnetic metal organic framework materials,^{54,55} and (3) the Co-O bonded interactions for the Co-bearing coordination polymer Co₃(C₈H₄O₄)₄(C₄H₁₂N)₂-(C₅H₁₁NO)₃,⁵⁶ the Co-O-bearing α -diimine microcyclic complex,⁵⁷ and paramagnetic CoO.⁵⁸ Given the structural complexities of several of the organic metallic complexes and the sometimes poorer quality and twinning of the crystals, it will be of interest to see the extent to which the experimental model properties agree with those calculated and the experimental values determined for the transition metal olivines and other structurally simpler materials such as CoO.⁵⁸ The degree to which the $G(\mathbf{r}_c)/\rho(\mathbf{r}_c)$ ratio and the total energy density, $H(\mathbf{r}_c)$, correlates with the experimental bond length will be examined. Also, the net atomic charges calculated for the transition metal atoms for the olivines will be compared with those conferred on the transition metal atoms in the organometallic complexes and sulfides. Finally, a comparison will be made of the local kinetic energy density estimated with the experimental model $\rho(\mathbf{r}_c)$ and $\nabla^2(\mathbf{r}_c)$ values and values calculated for the three transition metal olivines.

The $\rho(\mathbf{r}_c)$ and $\nabla^2\rho(\mathbf{r}_c)$ values calculated for Mn-O, Fe-O, and Co-O bonded interactions for the silicates and oxides (Table 2) are similar to one another for a given bond length and scatter roughly along parallel trends when plotted with respect to the experimental bond lengths (Figure 3). The values for both $\rho(\mathbf{r}_c)$ and $\nabla^2\rho(\mathbf{r}_c)$ scatter along similar trends for each of the bonded interactions with the values of $\rho(\mathbf{r}_c)$ increasing from 0.15 to 0.55 $e/\text{Å}^3$ (Figure 3a) and the values of $\nabla^2\rho(\mathbf{r}_c)$ increasing from 2.0 to 10.0 $e/\text{Å}^5$ as the experimental bond length

decreases from ~ 2.6 to ~ 2.0 Å (Figure 3b). For purposes of comparison, the $\nabla^2\rho(\mathbf{r}_c)$ values determined for the Ni-S bonded interactions for the nickel sulfides and for the Fe-S, and interactions for the iron sulfides are substantially smaller, ranging between 2 and 5 $e/\text{Å}^5$.^{13,59,60} In general, the trends displayed in Figure 3a show for a given bond length that a slightly greater accumulation of ED at the bcp is required for a Mn-O bonded interaction to adopt a given bond length than that required for a Fe-O bonded interaction. Furthermore, a greater accumulation is required for a Fe-O bonded interaction to adopt the given bond length than that required by a Co-O bonded interaction. The power law trend displayed in Figure 3b closely parallels the model experimental $\nabla^2\rho(\mathbf{r}_c)$ versus bond length trends reported by Poulsen et al.,⁵⁵ Overgaard et al.,⁵³ and Clausen et al.⁵⁶ for the Mn-O, Fe-O, and Co-O bonded interactions in organic metal complexes. The comparability of the experimental and the calculated Mn-O, Fe-O, and Co-O bcp properties may be expected given the similarities of the electronic configurations of the atoms, the similarity of the absolute electronegativities for Mn²⁺, Fe²⁺, and Co²⁺ cations (24.66, 23.42, and 25.28, respectively) compiled by Pearson,⁶¹ the close similarities of the X-ray photoelectron spectroscopy O1s loss satellites,⁶² and the X-ray absorption near-edge spectroscopy spectra at the metal K edges reported for MnO, FeO, and CoO,⁶³ respectively. The fact that the bond energies for the Mn-O (220.7 kcal/mol), Co-O (223.1 kcal/mol), and Fe-O (226.3 kcal/mol) bonds are close in value is further evidence that the bonded interactions can be expected to be similar.⁶⁴

As observed for the non-transition metal oxides, the ratio $G(\mathbf{r}_c)/\rho(\mathbf{r}_c)$ for the Mn-O, Fe-O, and Co-O interactions is

TABLE 2: Calculated Bond Critical Point and Local Energy Density Properties for Mn–O, Fe–O, and Co–O Bonded Interactions

$R(\text{Mn–O})$ (Å)	$\rho(\mathbf{r}_c)$ ($\text{e } \text{Å}^{-3}$)	$\nabla^2\rho(\mathbf{r}_c)$ ($\text{e } \text{Å}^{-5}$)	λ_1 ($\text{e } \text{Å}^{-5}$)	λ_2 ($\text{e } \text{Å}^{-5}$)	λ_3 ($\text{e } \text{Å}^{-5}$)	$G(\mathbf{r}_c)$ (au)	$V(\mathbf{r}_c)$ (au)
Glaucochroite, CaMnSiO_4 , Lager and Meagher ⁷¹							
2.159	0.4045	6.021	−1.715	−1.692	9.427	0.0721	−0.0817
2.218	0.3589	5.034	−1.432	−1.409	7.874	0.0603	−0.0685
2.251	0.3261	4.641	−1.307	−1.267	7.215	0.0545	−0.0608
2.251	0.3269	4.633	−1.311	−1.271	7.215	0.0544	−0.0609
2.159	0.4055	6.011	−1.722	−1.697	9.430	0.0720	−0.0818
Manganosite, MnO , Pacalo and Graham ⁷²							
2.222	0.3538	5.017	−1.330	−1.330	7.676	0.0601	−0.0682
Spessartine, $\text{Mn}_3\text{Al}_2\text{Si}_4\text{O}_{12}$, Rodehorst et al. ⁷³							
2.246	0.3308	4.750	−1.313	−1.309	7.372	0.0558	−0.0623
2.404	0.2295	3.154	−0.083	−0.786	4.767	0.0355	−0.0381
2.403	0.2300	3.147	−0.083	−0.788	4.765	0.0354	−0.0381
2.245	0.3316	4.739	−1.318	−1.314	7.371	0.0558	−0.0623
Tephroite, Mn_2SiO_4 , Francis and Ribbe ⁷⁴							
2.183	0.3755	5.676	−1.587	1.546	8.810	0.0669	−0.0749
2.140	0.4086	6.399	−1.847	1.777	10.020	0.0746	−0.0830
2.293	0.2932	4.143	−1.154	1.134	6.431	0.0478	−0.0527
2.143	0.4010	6.330	−1.787	1.718	9.835	0.0735	−0.0814
2.144	0.4178	6.310	−1.791	1.762	9.863	0.0756	−0.0859
2.234	0.3471	4.820	−1.378	1.335	7.534	0.0576	−0.0652
2.324	0.2789	3.780	−1.048	1.013	5.841	0.0439	−0.0486
Tephroite, Mn_2SiO_4 , Kirfel et al. ³⁴							
2.245	0.3274	4.741	−1.320	−1.287	7.348	0.0554	−0.0616
2.322	0.2738	3.837	−1.058	−1.042	5.937	0.0439	−0.0481
2.138	0.4087	6.404	−1.848	−1.783	10.04	0.0746	−0.0829
2.157	0.3894	6.057	−1.720	−1.651	9.428	0.0703	−0.0778
2.170	0.3966	5.817	−1.666	−1.636	9.119	0.0697	−0.0792
2.253	0.3345	4.536	−1.312	−1.272	7.120	0.0542	−0.0614
2.321	0.2815	3.796	−1.062	−1.030	5.888	0.0442	−0.0490
$R(\text{Fe–O})$ (Å)	$\rho(\mathbf{r}_c)$ ($\text{e } \text{Å}^{-3}$)	$\nabla^2\rho(\mathbf{r}_c)$ ($\text{e } \text{Å}^{-5}$)	λ_1 ($\text{e } \text{Å}^{-5}$)	λ_2 ($\text{e } \text{Å}^{-5}$)	λ_3 ($\text{e } \text{Å}^{-5}$)	$G(\mathbf{r}_c)$ (au)	$V(\mathbf{r}_c)$ (au)
Fayalite, Fe_2SiO_4 , Kirfel and Lippmann ³³							
2.122	0.4146	7.072	−1.713	−1.660	10.440	0.0806	−0.0879
2.232	0.3178	5.183	−1.187	−1.186	7.555	0.0567	−0.0597
2.065	0.4711	8.105	−2.156	−2.050	12.310	0.0937	−0.0103
2.110	0.4201	7.221	−1.775	−1.737	10.730	0.0817	−0.0885
2.125	0.4229	6.904	−1.741	−1.668	10.310	0.0798	−0.0881
2.236	0.3308	4.998	−1.234	−1.186	7.418	0.0560	−0.0601
2.293	0.2880	4.321	−1.041	−1.035	6.397	0.0473	−0.0497
Wustite, FeO , Fjellvag et al. ⁷⁵							
2.163	0.3809	6.324	−1.368	−1.368	9.059	0.0718	−0.0780
Kirschsteinite, CaFeSiO_4 , Folco and Mellini ⁷⁶							
2.138	0.4089	6.626	−1.672	−1.593	9.891	0.0762	−0.0837
2.193	0.3639	5.632	−1.397	−1.332	8.361	0.0640	−0.0697
2.233	0.3239	5.103	−1.239	−1.175	7.517	0.0565	−0.0601
2.233	0.3244	5.097	−1.241	−1.179	7.518	0.0564	−0.0601
2.138	0.4094	6.618	−1.675	−1.599	9.893	0.0762	−0.0837
Orthoferrosilite, FeSiO_3 , Sueno et al. ⁷⁷							
2.083	0.4485	7.947	−1.886	−1.860	11.690	0.0911	−0.0999
2.195	0.3446	5.777	−1.381	−1.291	8.448	0.0637	−0.0675
2.157	0.3790	6.370	−1.506	−1.472	9.348	0.0713	−0.0765
1.993	0.5631	9.896	−2.664	−2.596	15.160	0.0118	−0.0135
2.123	0.4078	7.126	−1.642	−1.620	10.390	0.0805	−0.0872
2.128	0.4068	6.854	−1.675	−1.622	10.150	0.0777	−0.0844
2.194	0.3453	5.776	−1.385	−1.304	8.465	0.0637	−0.0676
2.089	0.4326	7.682	−1.875	−1.788	11.340	0.0869	−0.0941
2.123	0.4050	6.964	−1.721	−1.647	10.330	0.0784	−0.0845
2.023	0.5357	8.945	−2.483	−2.425	13.850	0.0108	−0.1233
2.461	0.1971	2.892	−0.673	−0.510	4.075	0.0299	−0.0299
2.597	0.1410	1.987	−0.409	−0.391	2.799	0.0200	−0.0195
Almandine, $\text{Fe}_3\text{Al}_2\text{Si}_3\text{O}_{12}$, Armbruster et al. ⁷⁸							
2.222	0.3363	5.302	−1.322	−1.249	7.873	0.0591	−0.0633
2.371	0.2356	3.577	−0.815	−0.774	5.166	0.0378	−0.0386
2.221	0.3367	5.295	−1.325	−1.253	7.873	0.0591	−0.0633

TABLE 2: Continued

$R(\text{Co-O})$ (Å)	$\rho(\mathbf{r}_c)$ ($\text{e } \text{Å}^{-3}$)	$\nabla^2\rho(\mathbf{r}_c)$ ($\text{e } \text{Å}^{-5}$)	λ_1 ($\text{e } \text{Å}^{-5}$)	λ_2 ($\text{e } \text{Å}^{-5}$)	λ_3 ($\text{e } \text{Å}^{-5}$)	$G(\mathbf{r}_c)$ (au)	$V(\mathbf{r}_c)$ (au)
$\text{Co}_3\text{Al}_2\text{Si}_3\text{O}_{12}$, Taran ⁷⁹							
2.212	0.3382	2.552	-1.283	-1.236	7.771	0.0601	-0.0657
2.339	0.2527	8.335	-0.927	-0.867	5.629	0.0413	-0.0429
2.212	0.3385	2.548	-1.286	-1.239	7.773	0.0601	-0.0657
Co_2SiO_4 , Morimoto et al. ⁸⁰							
2.100	0.4226	7.141	-1.646	-1.604	10.390	0.0840	-0.0939
2.182	0.3450	5.742	-1.256	-1.216	8.215	0.0651	-0.0705
2.072	0.4518	7.493	-1.990	-1.813	11.300	0.0886	-0.0995
2.079	0.4388	7.496	-1.790	-1.691	10.980	0.0878	-0.0979
2.100	0.4364	6.985	-1.699	-1.683	10.370	0.0837	-0.0949
2.176	0.3671	5.717	-1.312	-1.277	8.306	0.0665	-0.0736
2.228	0.3277	4.965	-1.224	-1.182	7.372	0.0563	-0.0612
Co-Monticellite, CaCoSiO_4 , Kimata and Nishida ⁸¹							
2.134	0.4008	6.354	-1.503	-1.470	9.326	0.0749	-0.0839
2.188	0.3577	5.481	-1.256	-1.232	7.969	0.0637	-0.0705
2.219	0.3226	5.103	-1.177	-1.073	7.352	0.0576	-0.0623
2.134	0.4011	6.352	-1.513	-1.460	9.325	0.0749	-0.0839
CoO, Wyckoff ⁸²							
2.133	0.4332	6.277	-0.405	-0.405	7.087	0.0903	-0.1154

larger than unity (Figure 4a) (except for one Fe–O bonded interaction), each increasing with decreasing bond length (from 2.6 to 2.0 Å) from a value of ~ 0.95 au e^{-1} to a value of ~ 1.4 au e^{-1} . Concomitant with the trend, the total energy density, $H(\mathbf{r}_c)$, decreases from ~ 0.0 to -0.015 au (Figure 4b), a result indicating that the shared interaction for the three bonded interaction increases as the bond lengths decrease, and the ED is progressively accumulated at \mathbf{r}_c and $\nabla^2\rho(\mathbf{r}_c)$ increases in value.

Unlike the trends displayed by the $G(\mathbf{r}_c)/\rho(\mathbf{r}_c)$ data sets, the total energy density values scatter along three largely disjoint trends (Figure 4b). The $H(\mathbf{r}_c)$ values for the bulk of the Mn–O, Co–O, and Fe–O interactions are negative, so the shared character of the bonded interactions is largely confirmed.² Furthermore, the decrease in $H(\mathbf{r}_c)$ for a given bond length in the order Fe–O, Co–O, and Mn–O is consistent with the trends in Figure 4a, where for a given bond length, a larger accumulation of ED is

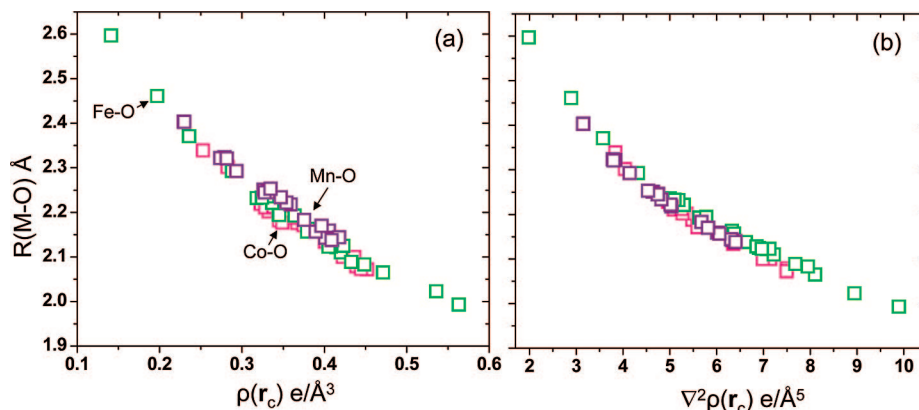


Figure 3. Experimental M–O bond lengths, $R(\text{M-O})$ ($M = \text{Mn, Fe, Co}$), plotted with respect to (a) $\rho(\mathbf{r}_c)$ and (b) $\nabla^2\rho(\mathbf{r}_c)$ calculated for a variety of Mn–O- (violet squares), Fe–O- (green squares), and Co–O-bearing (pink squares) silicates and oxides.

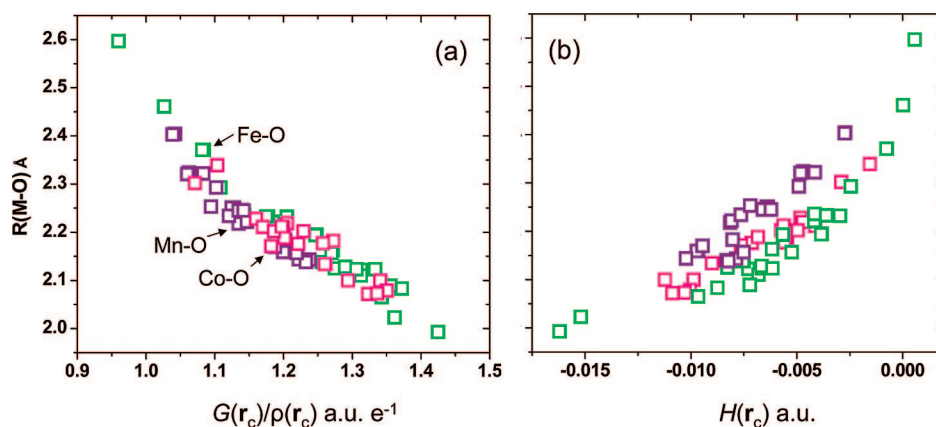


Figure 4. Experimental M–O bond length, $R(\text{M-O})$ ($M = \text{Mn, Fe, Co}$) plotted with respect to (a) $G(\mathbf{r}_c)/\rho(\mathbf{r}_c)$ and (b) $H(\mathbf{r}_c)$ calculated for the transition metal materials used to construct Figure 3 (see caption of Figure 3 for definition of symbols).

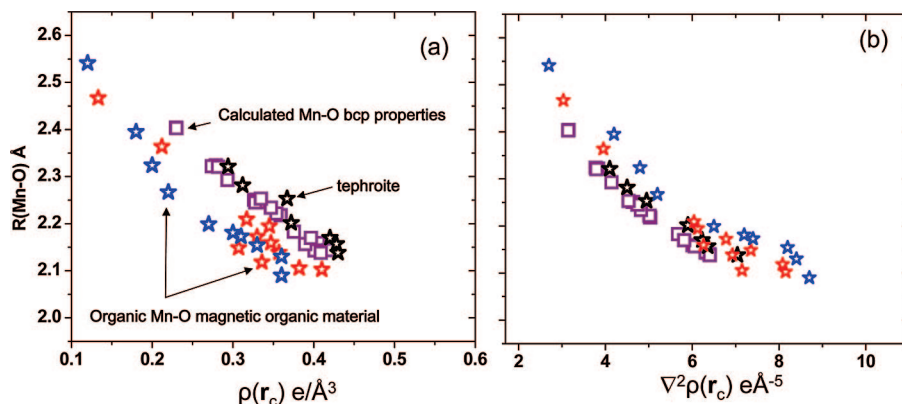


Figure 5. Experimental $R(\text{Mn–O})$ plotted with respect to (a) $\rho(\mathbf{r}_c)$ and (b) $\nabla^2\rho(\mathbf{r}_c)$ values (violet squares) calculated for a variety of Mn–O-bearing silicates and oxides (used to construct Figure 3) compared with experimental model $\rho(\mathbf{r}_c)$ and $\nabla^2\rho(\mathbf{r}_c)$ values determined for tephroite (black stars),³⁴ for the magnetic metal–organic magnetic framework materials $\text{Mn}_2(\text{C}_8\text{H}_4\text{O}_4)_2(\text{C}_3\text{H}_7\text{NO})_2$ (blue stars),⁵⁴ and for $[\text{Mn}_3(\text{C}_8\text{O}_4\text{H}_4)_3(\text{C}_5\text{H}_{11}\text{ON})_2]$ (red stars).⁵⁵

required for a Mn–O bonded interaction to adopt a given bond length than is required for a Co–O bonded interaction.

It is noteworthy that the values for $G(\mathbf{r}_c)/\rho(\mathbf{r}_c)$ reported for the two magnetic Mn–O organic framework materials^{54,55} increase linearly from 1.25 to 1.55 au e^{-1} as $R(\text{Mn–O})$ decreases from 2.55 to 2.10 Å. The values reported for the Fe–O bonded interactions for the three redox active mixed valence trinuclear oxo-centered Fe-centered carboxylates studied by Overgaard et al.⁵³ also increase linearly with $R(\text{Fe–O})$ from 1.46 to 1.70 au e^{-1} as $R(\text{Fe–O})$ decreases from 2.01 to 1.83 Å. Furthermore, the $G(\mathbf{r}_c)/\rho(\mathbf{r}_c)$ ratio tends to increase (from ~ 1.4 to $\sim 1.6 \text{ au e}^{-1}$) with decreasing bond length (from 2.10 to 1.95 Å) for the Co–O bonded interactions for the Co-bearing coordination polymer⁵⁶ $\text{Co}_3(\text{C}_8\text{H}_4\text{O}_4)_4(\text{C}_4\text{H}_{12}\text{N})_2(\text{C}_5\text{H}_{11}\text{NO})_3$. However, the trend is much more poorly developed. These trends indicate that the shared character of the M–O bonded interactions for these materials increases as $\rho(\mathbf{r}_c)$ and $\nabla^2\rho(\mathbf{r}_c)$ both increase in value. The increase of the $G(\mathbf{r}_c)/\rho(\mathbf{r}_c)$ ratio with decreasing bond length and $H(\mathbf{r}_c)$ appears to be a general relationship that holds not only for a number of non-transition and transition M–O bonded interactions but also for Co–Co and C–C bonded interactions (see above) and perhaps in general. As observed for the non-transition metal M–O bonded interactions, $\nabla^2\rho(\mathbf{r}_c)$ is observed to increase in value for the transition M–O bonded interactions as $\rho(\mathbf{r}_c)$ increases in value.

The $\rho(\mathbf{r}_c)$ and $\nabla^2\rho(\mathbf{r}_c)$ values calculated for the Mn–O bonded interaction are compared in Figure 5 with the experimental model values for the Mn–O bonded interactions reported for tephroite³⁴ and for the magnetic metal–organic magnetic framework materials $\text{Mn}_2(\text{C}_8\text{H}_4\text{O}_4)_2(\text{C}_3\text{H}_7\text{NO})_2$ ⁵⁴ and $[\text{Mn}_3(\text{C}_8\text{O}_4\text{H}_4)_3(\text{C}_5\text{H}_{11}\text{ON})_2]$.⁵⁵ The experimental values for $\rho(\mathbf{r}_c)$ for tephroite are comparable with the calculated values, with one value falling slightly outside the trend of the calculated values (Figure 5a). The $\nabla^2\rho(\mathbf{r}_c)$ values are also comparable, paralleling but slightly larger than the calculated values (Figure 5b). Overall, the agreement between the experimental $\rho(\mathbf{r}_c)$ and $\nabla^2\rho(\mathbf{r}_c)$ values for tephroite and the calculated values is considered to be moderately good. The agreement of the experimental bcp properties reported for the two metal–organic framework complexes is somewhat poorer. The experimental $\rho(\mathbf{r}_c)$ values roughly parallel the calculated trend, but they are $\sim 0.1 \text{ e}/\text{Å}^3$ smaller in value than the calculated ones. The experimental $\nabla^2\rho(\mathbf{r}_c)$ values also parallel the calculated trend, but they tend to be $\sim 1.0 \text{ e}/\text{Å}^5$ larger than the calculated values (Figure 5b). Nonetheless, given the poor quality of some of the metal–organic crystals and the much greater complexities of the organic

framework structures,^{54,55} the agreement is considered to be relatively good, particularly for the $\nabla^2\rho(\mathbf{r}_c)$ data.

The experimental $\rho(\mathbf{r}_c)$ values for the Fe–O bonded interactions for fayalite³³ and the three redox active mixed valence trinuclear oxo-centered iron carboxylates⁵³ and an oxidized trinuclear iron complex $[\text{Fe}_3\text{O}(\text{HCOO})_6(\text{HCOO})_3]\cdot\text{H}_2\text{O}\cdot 2(2\text{CH}_3\text{NC}_5\text{H}_5)$ ⁵⁶ are in good agreement, with the experimental values falling within and beyond the trend of the calculated $\rho(\mathbf{r}_c)$ values (Figure 6a). The $\nabla^2\rho(\mathbf{r}_c)$ values observed for fayalite are in relatively close agreement with the calculated values, whereas the values observed for the three iron carboxylates are in poorer agreement, with two values displaced from the trend of the calculated values (Figure 6b). Again, given the complexities of the structures of the three iron carboxylates and the trinuclear iron complex compared with that of fayalite, the overall agreement of the experimental and calculated $\rho(\mathbf{r}_c)$ values is considered to be good. Despite the value $\nabla^2\rho(\mathbf{r}_c)$ being a second derivative of $\rho(\mathbf{r}_c)$, the agreement of the experimental model $\nabla^2\rho(\mathbf{r}_c)$ values with the calculated values is also good. The agreement of the experimental bcp properties, collected at 15 K for the oxidized trinuclear iron complex, with the calculated values is considered to be particularly good, a testament to the care that Professor Bo Brummerstedt Iversen and his colleagues exercised in collecting and modeling the synchrotron single-crystal diffraction data.

The agreement of the experimental and calculated $\rho(\mathbf{r}_c)$ and $\nabla^2\rho(\mathbf{r}_c)$ values for the Co–O bonded interactions for the Co_2SiO_4 olivine,³⁵ CoO ⁵⁸ and the α -diimine microcyclic complex $\text{Co}(\text{C}_{12}\text{H}_{20}\text{N}_8)(\text{H}_2\text{O})_2\cdot 2\text{ClO}_4$ ⁵⁷ is good for the most part, despite α -diimine's being a relatively complex molecular structure linked together by water molecules and perchlorate anions. In contrast, the agreement of the experimental model $\rho(\mathbf{r}_c)$ value reported for the Co-bearing coordination polymer $\text{Co}_3(\text{C}_8\text{H}_4\text{O}_4)_4(\text{C}_4\text{H}_{12}\text{N})_2(\text{C}_5\text{H}_{11}\text{NO})_3$ ⁵⁶ is relatively poor (Figure 7a), whereas the agreement of the experimental $\nabla^2\rho(\mathbf{r}_c)$ values is surprisingly good, particularly given the poorer agreement of the experimental model $\rho(\mathbf{r}_c)$ values and the tendency of the polymer crystals to twin. The model $\rho(\mathbf{r}_c)$ values observed for the Co_2SiO_4 olivine scatter largely within the scatter of the calculated $R(\text{Co–O}) - \rho(\mathbf{r}_c)$ data set. The experimental model $\nabla^2\rho(\mathbf{r}_c)$ values likewise scatter along the trend for the calculated $R(\text{Co–O}) - \nabla^2\rho(\mathbf{r}_c)$ data, although slightly displaced. Overall, as observed for the other olivines forsterite, fayalite, and tephroite, the agreement of the model experimental $\rho(\mathbf{r}_c)$ and $\nabla^2\rho(\mathbf{r}_c)$ values for the Co_2SiO_4 olivine with the calculated values is considered to be good.

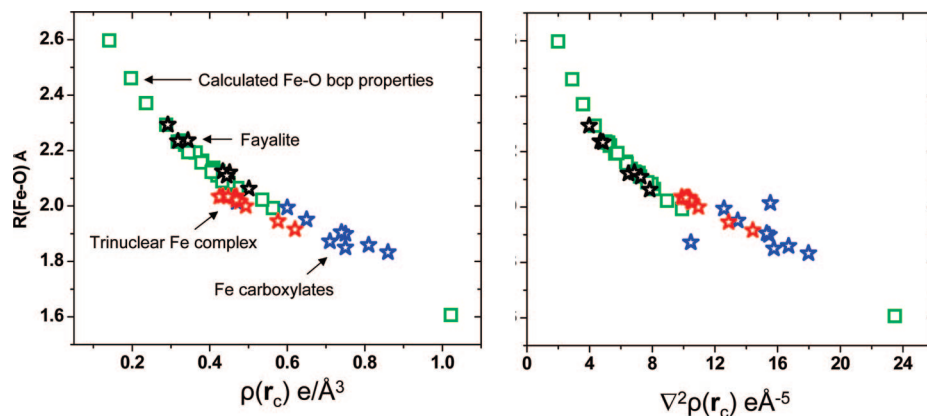


Figure 6. Experimental $R(\text{Fe}-\text{O})$ plotted with respect to (a) $\rho(\mathbf{r}_c)$ and (b) $\nabla^2\rho(\mathbf{r}_c)$ values (green squares) calculated for a variety of Fe-O-bearing silicates and oxides (used to construct Figure 3) compared with experimental model $\rho(\mathbf{r}_c)$ and (b) $\nabla^2\rho(\mathbf{r}_c)$ values determined for fayalite (black stars),³³ for trinuclear oxo-centered iron carboxylate, $[\text{Fe}_3\text{O}(\text{CH}_2\text{ClCOO})_6(\text{H}_2\text{O})_3]\cdot 3\text{H}_2\text{O}$, its oxidized form $[\text{Fe}_3\text{O}(\text{CH}_2\text{ClCOO})_6(\text{H}_2\text{O})_2\text{-(CH}_2\text{ClCOO)}]\cdot \text{H}_2\text{O}$, and $\text{Fe}_3\text{O}(\text{C}(\text{CH}_3)_3\text{COO})_6(\text{NC}_5\text{H}_5)_3$ (blue stars),⁵³ and for oxidized trinuclear iron complex $[\text{Fe}_3\text{O}(\text{HCOO})_6(\text{HCOO})_3]\cdot \text{H}_2\text{O}\cdot 2(2\text{CH}_3\text{NC}_5\text{H}_5)$ (red stars).⁵³

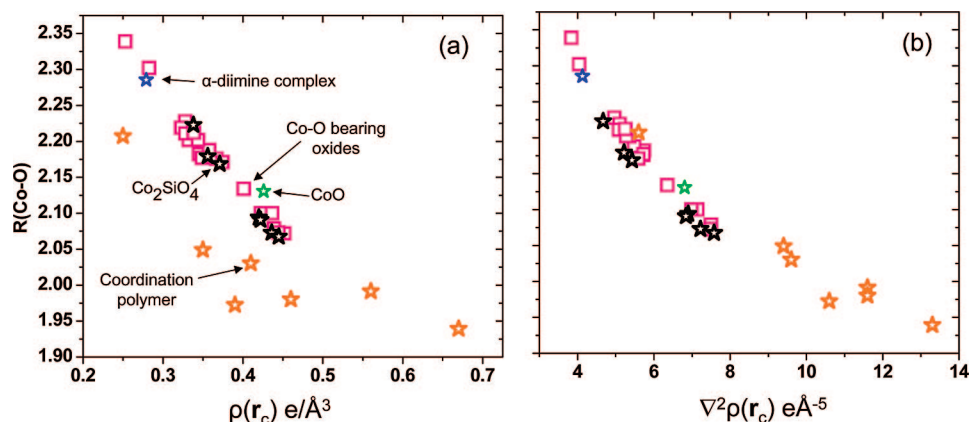


Figure 7. Experimental Co-O bond lengths, $R(\text{Co}-\text{O})$, plotted with respect to (a) $\rho(\mathbf{r}_c)$ and (b) $\nabla^2\rho(\mathbf{r}_c)$ values (pink squares) calculated for a variety of Co-O-bearing silicates and oxides (used to construct Figure 3) compared with experimental model $\rho(\mathbf{r}_c)$ and (b) $\nabla^2\rho(\mathbf{r}_c)$ values determined for Co_2SiO_4 (black stars),³⁵ CoO (green star),⁵⁸ α -diimine (blue star),⁵⁷ and for the microcyclic complex $[\text{Co}(\text{C}_{12}\text{H}_{20}\text{N}_8)(\text{H}_2\text{O})_2]\cdot 2\text{ClO}_4$ (orange stars).⁵⁶

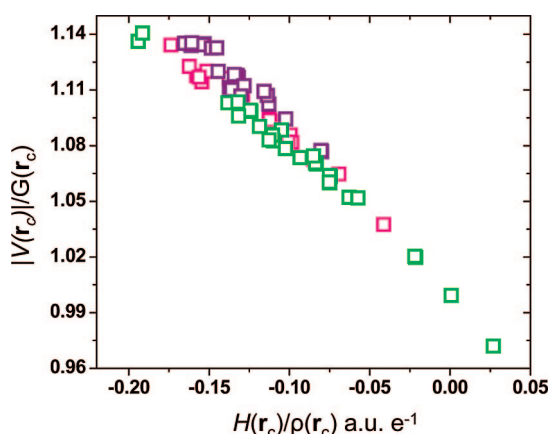


Figure 8. Espinosa's⁴⁹ $IV(\mathbf{r}_c)/G(\mathbf{r}_c)$ bond character indicator plotted with respect to the bond degree ratio $H(\mathbf{r}_c)/\rho(\mathbf{r}_c)$ for the Mn-O, Fe-O, and Co-O bonded interactions with the $V(\mathbf{r}_c)$, $G(\mathbf{r}_c)$, $H(\mathbf{r}_c)$, and $\rho(\mathbf{r}_c)$ calculated for the Mn-O-, Fe-O-, and Co-O-bearing silicates and oxides.

The $IV(\mathbf{r}_c)/G(\mathbf{r}_c)$ bond character indicator ratio for the calculated Mn-O, Fe-O, and Co-O bonded interactions, as defined by Espinosa et al.,⁴⁹ is plotted in Figure 8 with respect to the bond degree factor $H(\mathbf{r}_c)/\rho(\mathbf{r}_c)$ (interpreted by Espinosa⁴⁹ as the total energy per electron at \mathbf{r}_c). On the basis of the bond degree factor, the bonded interactions are indicated to be largely

intermediate in character with a substantial component of closed-shell character, with one of the Fe-O interactions having a $IV(\mathbf{r}_c)/G(\mathbf{r}_c)$ ratio of less than 1.0, the boundary between a closed-shell and an intermediate interaction. The $IV(\mathbf{r}_c)/G(\mathbf{r}_c)$ ratios reported for the Fe-S and Cu-S bonded interactions for several sulfides fall between 1.2 and 1.6 and $H(\mathbf{r}_c)/\rho(\mathbf{r}_c)$ ratios between -0.2 and -0.4 au e^{-1} ,⁶⁰ supporting a view that M-S bonded interactions have a larger component of shared character than the transition M-O interactions.

Estimates of the Local Kinetic Energy Density Properties.

There is no way to determine the local kinetic energy, $G(\mathbf{r}_c)$, directly from an experimental electron density distribution, short of finding the Hohenberg-Kohn universal functional⁶⁵ or at least its component that determines $G(\mathbf{r}_c)$ in terms of $\rho(\mathbf{r}_c)$.⁶⁶ It can be estimated, however, for a given bonded interaction with the corrected electron gas theory approximation $\langle G(\mathbf{r}_c) \rangle = (3/10)(3\pi^2)^{2/3}\rho(\mathbf{r}_c)^{5/3} + 1/6\nabla^2\rho(\mathbf{r}_c)$ (all variables are in au).³⁹ Using the calculated values for $\rho(\mathbf{r}_c)$ and $\nabla^2\rho(\mathbf{r}_c)$, $\langle G(\mathbf{r}_c) \rangle$ was estimated and compared with the calculated local kinetic energies, $G(\mathbf{r}_c)$ (Figure 9a). Although the estimated values are highly correlated with $G(\mathbf{r}_c)$, they are systematically slightly smaller than the values of $G(\mathbf{r}_c)$. A similar agreement between $G(\mathbf{r}_c)$ and $\langle G(\mathbf{r}_c) \rangle$ was reported earlier for the non-transition M-O bonded interactions.⁴⁰ As the local kinetic energy is expected to increase with decreasing bond length and increasing ED at \mathbf{r}_c , $G(\mathbf{r}_c)$ is

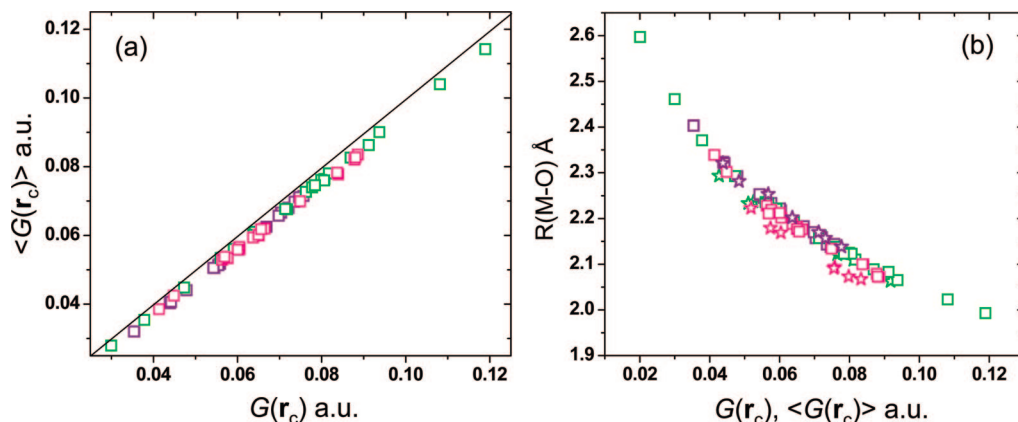


Figure 9. (a) $\langle G(\mathbf{r}_c) \rangle$ calculated with the corrected electron gas theory approximation $\langle G(\mathbf{r}_c) \rangle = (3/10)(3\pi^2)^{2/3}\rho(\mathbf{r}_c)^{5/3} + 1/6\nabla^2\rho(\mathbf{r}_c)$ (all variables are in au)³⁹ using the $\rho(\mathbf{r}_c)$ and $\nabla^2\rho(\mathbf{r}_c)$ values calculated with Mn–O-, Fe–O-, and Co–O-bearing silicates and oxides plotted with respect to $G(\mathbf{r}_c)$ (see the caption of Figure 3 for definition of symbols). (b) Experimental bond lengths $R(\text{M–O})$ plotted with respect to calculated values of $G(\mathbf{r}_c)$ (squares) and with respect to $\langle G(\mathbf{r}_c) \rangle$ calculated using the experimental $\rho(\mathbf{r}_c)$ and $\nabla^2\rho(\mathbf{r}_c)$ values for tephroite (violet stars), fayalite (green stars), and Co_2SiO_4 olivine (pink stars).

expected to increase with decreasing bond length. As displayed in Figure 9b, the $G(\mathbf{r}_c)$ values for the Fe–O, Mn–O, and Co–O bonded interactions roughly scatter along nonlinearly parallel trends with decreasing bond length. Furthermore, the $\langle G(\mathbf{r}_c) \rangle$ values estimated with the experimental model $\rho(\mathbf{r}_c)$ and $\nabla^2\rho(\mathbf{r}_c)$ values for the Mn–O bonded interactions of tephroite and for the Fe–O interactions of fayalite cluster largely within the trend defined by the $R(\text{M–O}) - G(\mathbf{r}_c)$ trend, with the values determined for the Co–O interactions paralleling but slightly offset from the trend (Figure 9b). Nonetheless, the close agreement between the experimental $\langle G(\mathbf{r}_c) \rangle$ values and the estimated $G(\mathbf{r}_c)$ values displayed in the figure attests to the validity of the corrected electron gas theory approximation.

Atomic Charges. An integration of the ED over the basins of the nonequivalent atoms for tephroite resulted in the chemical formula $\text{Mn}(1)^{1.61+}\text{Mn}(2)^{1.67+}\text{Si}^{3.44+}\text{O}(1)^{1.75-}\text{O}(2)^{1.66-}\text{O}(3)_2^{1.64-}$, that for fayalite resulted in $\text{Fe}(1)^{1.36+}\text{Fe}(2)^{1.48+}\text{Si}^{3.20+}\text{O}(1)^{1.52-}\text{O}(2)^{1.57-}\text{O}(3)_2^{1.47-}$, and that for the Co_2SiO_4 olivine resulted in $\text{Co}(1)^{1.31+}\text{Co}(2)^{1.30+}\text{Si}^{3.25+}\text{O}(1)^{1.42-}\text{O}(2)^{1.59-}\text{O}(3)_2^{1.51-}$. As evinced by the formulas, the atomic charges conferred on the transition metal atoms decrease with increasing atomic number from $\text{Mn}(1)^{1.61+}\text{Mn}(2)^{1.67+}$ to $\text{Fe}(1)^{1.36+}\text{Fe}(2)^{1.48+}$ to $\text{Co}(1)^{1.31+}\text{Co}(2)^{1.30+}$. An integration of the ED within a sphere determined by the radial ED distribution of the atoms for tephroite⁶⁷ resulted in the chemical formula $\text{Mn}(1)^{0.99+}\text{Mn}(2)^{0.99+}\text{Si}^{1.05+}\text{O}(1)^{1.01-}\text{O}(2)^{1.02-}\text{O}(3)_2^{1.01-}$, a result which suggests that the bonded interactions are more shared in character than that indicated by an integration of the ED over the basin of the atoms. The net atomic charges, $\sim +2.035$, conferred on the Mn atoms in $\text{Mn}_2(\text{C}_8\text{H}_4\text{O}_4)_2(\text{C}_3\text{H}_7\text{NO})_2$ ⁵⁴ are larger than those conferred on the Mn atoms in tephroite and in close agreement with the nominal charge of 2+ for the Mn^{2+} cation. The charges conferred on the Co atoms for the Co-bearing coordination polymer $\text{Co}_3(\text{C}_8\text{H}_4\text{O}_4)_4(\text{C}_4\text{H}_{12}\text{N}_2)(\text{C}_5\text{H}_{11}\text{NO})_3$,⁵⁶ $q(\text{Co}^{\text{IV}}(1)) = +1.88$ and $q(\text{Co}^{\text{VI}}(2)) = +1.91$, are substantially larger than those conferred on the Co atoms in Co_2SiO_4 . Note that also the atomic charge on the six-coordinate Co atom is slightly larger than that conferred on the four-coordinate Co. The atomic charges conferred on the Fe atoms in fayalite are substantially larger than those conferred on the high spin state Fe atoms in troilite $\text{Fe}^{0.81+}\text{S}^{0.81-}$ and the low spin state Fe atoms in marcasite and pyrite $\text{Fe}^{0.67+}\text{S}_2^{0.34-}$,⁶⁰ as one might expect from electronegativity considerations and the $|V(\mathbf{r}_c)|/G(\mathbf{r}_c)$ ratios.

The net charges conferred on the Si atoms for the three olivines (+3.30 e, on average) are larger than those conferred

on the six coordinated Si atoms in stishovite +3.21 e, $\text{SiO}_2\text{--II}$, +3.20 e, and $\text{SiO}_2\text{--III}$, +3.17 e,⁶⁸ a result indicating that the characters of the Si–O bonded interactions in SiO_4 and SiO_6 coordination polyhedra are basically the same and independent of the coordinate number of the Si atom.³¹ This is an unexpected result given that several studies indicate that the shared character of a bonded interaction increases with decreasing coordination number.^{46–48}

Concluding Remarks

The trends displayed by the calculated bond critical point and local energy density properties for Mn–O, Fe–O, and Co–O bonded interactions for the olivines are not only comparable with one another but are also comparable with those observed for the non-transition M–O bonded interactions and those displayed by selected organometallic complexes. Indeed, the olivine results are considered to be noteworthy considering that they were obtained for different crystals, on several different stations, at different times, and with different resolutions. Despite the different conditions and materials, the agreement of the properties of the experimental model ED distributions for the Mg–O, Mn–O, Fe–O, and Co–O bonded interactions and those calculated turned out to be as good as may be expected. As $\nabla^2\rho(\mathbf{r}_c)$ increases, the value of $\rho(\mathbf{r}_c)$ increases for the olivines and $H(\mathbf{r}_c)$ decreases linearly as observed for the non-transition metal oxides with $\rho(\mathbf{r}_c)$ increasing in value as $H(\mathbf{r}_c)$ becomes progressively more negative in value. Also, as observed for the non-transition M–O bonded interaction, the ratio $G(\mathbf{r}_c)/\rho(\mathbf{r}_c)$ is greater than one (except for one Fe–O bonded interaction) and increases linearly with $R(\text{M–O})$ as $H(\mathbf{r}_c)$ decreases and becomes progressively more negative and the shared character of the bonded interactions increases. On the basis of this result, it appears that the $G(\mathbf{r}_c)/\rho(\mathbf{r}_c)$ may be a general measure of the shared character for a given bonded interaction: the greater the ratio for a given interaction, the more negative the value of $H(\mathbf{r}_c)$ and the more shared the interaction. The bulk of the transition metal bonded interactions qualify as intermediate interactions with the $|V(\mathbf{r}_c)|/G(\mathbf{r}_c)$ ratio ranging between 0.98 and 1.14, a result indicating that the bonded interactions are of intermediate character with a substantial component of closed-shell character. However, the $|V(\mathbf{r}_c)|/G(\mathbf{r}_c)$ ratio is smaller than that observed for the Fe–S bonded interactions⁵⁹ that range between 1.2 and 1.5 and the Ni–S interactions⁵⁹ that range between 1.2 and 1.4. On the basis of electronegativity considerations, the Fe–S is

expected to be a more shared interaction than an Fe–O interaction as indicated by its larger $|V(\mathbf{r}_c)|/G(\mathbf{r}_c)$ ratio.

The correspondence reported in this account between the properties of the non-transition and transition metal M–O bonded interactions in silicates and oxides, representative molecules, and the organometallic complexes suggests that a given M–O bonded interaction has intrinsically the same properties regardless of whether it occurs in an inorganic material, an organic complex, or a molecule, a result suggesting that the bonded interactions are governed in large part by local forces as asserted by Gibbs⁶⁹ and Hoffmann.⁷⁰ Finally, the overall agreement between the properties of the experimental model ED distributions and those calculated for the olivines, stishovite, and coesite indicates that first principles quantum mechanical calculations show great promise not only as a powerful tool in advancing our understanding of bonded interactions but also in clarifying the connection between the bond critical point and local energy properties, crystal structure, and the reactivity of earth materials.¹³

Acknowledgment. We thank the National Science Foundation (NSF) and the U.S. Department of Energy for supporting this study with Grants EAR-0609885 (N.L.R. and G.V.G.), EAR-0609906 (R.T.D.), and DE-FG02-97ER14751 (D.F.C.). K.M.R. acknowledges a grant from the U.S. Department of Energy (DOE), Office of Basic Energy Sciences, Geosciences Division, and computational facilities and support from the Environmental Molecular Sciences Laboratory (EMSL) at the Pacific Northwest National Laboratory (PNNL). The computations were performed in part at the EMSL at PNNL. The EMSL is a national scientific user facility sponsored by the U.S. DOE Office of Biological and Environmental Research. PNNL is operated by Battelle for the DOE under Contract DE-AC06-76RLO 1830. A.K. gratefully acknowledges financial support by the Bundesminister für Bildung und Forschung, Contract KS1 PDA. T.D.C. was supported by a grant from the NSF (CHE-0715185), a Cottrell Scholar Award from the Research Corporation, and a subcontract from Oak Ridge National Laboratory by Scientific Discovery through the AcIDAC program of the DOE under Contract DE-AC05-00OR22725 with Oak Ridge National Laboratory. G.V.G. takes pleasure in thanking Bob Downs for inviting him to visit the University of Arizona during the winter of 2008, where the bulk of the paper was written. We also thank the two reviewers for making several valuable suggestions that led to a substantial improvement of the paper.

References and Notes

- Coulson, C. A. *J. Chem. Soc.* **1955**, 2069.
- Cremer, D.; Kraka, E. *Croat. Chem. Acta* **1984**, *57*, 1259.
- Bader, R. F. W. There are no bonds—only bonding! In *Frontiers in Chemistry Series: Case Western Reserve University*; McMaster University: Hamilton, Canada, 2008.
- Pauling, L. *The Nature of the Chemical Bond*; Cornell University Press: Ithaca, NY, 1939.
- Coulson, C. A. *The Spirit of Applied Mathematics*; Clarendon Press: Oxford, U.K., 1953.
- Bader, R. F. W. *Atoms in Molecules*; Oxford Science Publications: Oxford, U.K., 1990.
- Parr, R. G.; Yang, W. *Density-Functional Theory of Atoms and Molecules*; Oxford University Press: Oxford, U.K., 1989.
- Bader, R. F. W. Molecular charge distributions, their display and use. In *Theoretical Chemistry*; Coulson, C. A., Buckingham, D. A., Eds.; Butterworth: London, U.K., 1975; Vol. II, pp 43.
- Runtz, G. R.; Bader, R. F. W.; Messer, R. R. *Can. J. Chem.—Rev. Can. Chim.* **1977**, *55*, 3040.
- Bader, R. F. W. *Acc. Chem. Res.* **1985**, *18*, 9.
- Bader, R. F. W. *J. Phys. Chem. A* **1998**, *102*, 7314.
- Gibbs, G. V.; Boisen, M. B.; Beverly, L. L.; Rosso, K. M. A computational quantum chemical study of the bonded interactions in earth materials and structurally and chemically related molecules. In *Molecular Modeling Theory: Applications in the Geosciences*; Cygan, R. T., Kubicki, J. D., Eds.; Mineralogical Society of America: Washington, DC, 2001; Vol. 42, pp 345.
- Gibbs, G. V.; Downs, R. T.; Cox, D. F.; Rosso, N. L.; Prewitt, C. T.; Rosso, K. M.; Lippmann, T.; Kirfel, A. Z. *Kristallogr.* **2008**, *223*, 1.
- Saunders, V. R.; Dovesi, R.; Roetti, C.; Causa, M.; Harrison, N. M.; Orlando, R.; Apra, E. *CRYSTAL98 User's Manual*; University of Torino: Torino, Italy, 1998.
- Gatti, C. *TOPOND96 User's Manual*; CNR-CSRSC: Milano, Italy, 1997.
- Gatti, C. Z. *Kristallogr.* **2005**, *220*, 399.
- Pendas, A. M.; Francisco, E.; Blanco, M. A.; Gatti, C. *Chem.—Eur. J.* **2007**, *13*, 9362.
- Downs, J. W.; Swope, R. J. *J. Phys. Chem.* **1992**, *96*, 4834.
- Stewart, R. *Acta Crystallogr., Sect. A* **1976**, *32*, 565.
- Stewart, R. F.; Spackman, M. A.; Flensburg, C. *VALRAY User's Manual*; Carnegie Mellon University and University of Copenhagen: Pittsburgh, PA, and Copenhagen, Denmark, 2000.
- Gibbs, G. V.; Cox, D. F.; Rosso, K. M.; Kirfel, A.; Lippmann, T.; Blaha, P.; Schwarz, K. *Phys. Chem. Miner.* **2005**, *32*, 114.
- Downs, J. W. *J. Phys. Chem.* **1995**, *99*, 6849.
- Kirfel, A.; Gibbs, G. V. *Phys. Chem. Miner.* **2000**, *27*, 270.
- Whitten, A. E.; Dittrich, B.; Spackman, M. A.; Turner, P.; Brown, T. C. *Dalton Trans.* **2004**, 23.
- Gibbs, G. V.; Whitten, A. E.; Spackman, M. A.; Stimpfl, M.; Downs, R. T.; Carducci, M. D. *J. Phys. Chem. B* **2003**, *107*, 12996.
- Lippmann, T.; Schneider, J. R. *Acta Crystallogr., Sect. A* **2000**, *56*, 575.
- Kirfel, A.; Krane, H. G.; Blaha, P.; Schwarz, K.; Lippmann, T. *Acta Crystallogr., Sect. A* **2001**, *57*, 663.
- Coppens, P.; Iversen, B.; Larsen, F. K. *Coord. Chem. Rev.* **2005**, *249*, 179.
- Koritsanszky, T. S.; Coppens, P. *Chem. Rev.* **2001**, *101*, 1583.
- Kuntzinger, S.; Ghermani, N. E.; Dusaosoy, Y.; Lecomte, C. *Acta Crystallogr. Sect. B: Struct. Sci.* **1998**, *54*, 819.
- Bianchi, R.; Forni, A.; Oberti, R. *Phys. Chem. Miner.* **2005**, *32*, 638.
- Kirfel, A.; Lippmann, T.; Blaha, P.; Schwarz, K.; Cox, D. F.; Rosso, K. M.; Gibbs, G. V. *Phys. Chem. Miner.* **2005**, *32*, 301.
- Kirfel, A.; Lippmann, T. Electron density distribution in fayalite, Fe₂SiO₄: a high energy synchrotron radiation study; HASYLAB, 2002.
- Kirfel, A.; Lippmann, T.; Morgenroth, W. Electron density distribution in tephroite, Mn₂SiO₄: a high energy synchrotron radiation study; HASYLAB, 2003.
- Lippmann, T.; Morgenroth, W.; Kirfel, A. Electron density distribution in Co-olivine, Co₂SiO₄, from D3 and BW5 data; HASYLAB, 2004.
- Tsirelson, V. G. Interpretation of experimental electron densities by combination of the QTAMC and DFT. In *The Quantum Theory of Atoms in Molecules*; Matta, C. F., Boyd, R. J., Eds.; Wiley-VCH Verlag: Weinheim, Germany, 2007; pp 257.
- Volkov, A.; Coppens, P. *Acta Crystallogr., Sect. A* **2001**, *57*, 395.
- Hirshfeld, F. L. *Israel J. Chem.* **1977**, *16*, 226.
- Kirzhnits, D. A. *Sov. Phys. JETP* **1957**, *5*, 64.
- Gibbs, G. V.; Spackman, M. A.; Jayatilaka, D.; Rosso, K. M.; Cox, D. F. *J. Phys. Chem. A* **2006**, *110*, 12259.
- Bone, R. G. A.; Bader, R. F. W. *J. Phys. Chem.* **1996**, *100*, 10892.
- Cortes-Guzman, F.; Bader, R. F. W. *Coord. Chem. Rev.* **2005**, *249*, 633.
- Bader, R. F. W.; Essen, H. *J. Chem. Phys.* **1984**, *80*, 1943.
- Macchi, P.; Sironi, A. *Coord. Chem. Rev.* **2003**, *238–239*, 383.
- Stash, A. I.; Tanaka, K.; Shiozawa, K.; Makino, H.; Tsirelson, V. G. *Acta Crystallogr. Sect. B* **2005**, *61*, 418.
- Mooser, E.; Pearson, W. B. *Acta Crystallogr.* **1959**, *12*, 1015.
- Phillips, J. C. *Rev. Mod. Phys.* **1970**, *42*, 317.
- Shankar, S.; Parr, R. G. *Proc. Natl. Acad. Sci. U.S.A.* **1985**, *82*, 264.
- Espinosa, E.; Alkorta, I.; Elguero, J.; Molins, E. *J. Chem. Phys.* **2002**, *117*, 5529.
- Bianchi, R.; Gervasio, G.; Marabello, D. *Inorg. Chem.* **2000**, *39*, 2360.
- Gatti, C.; Lasi, D. *Faraday Discuss.* **2007**, *135*, 55.
- Knop, O.; Rankin, K. N.; Boyd, R. J. *J. Phys. Chem. A* **2003**, *107*, 272.
- Overgaard, J.; Larsen, F. K.; Schiott, B.; Iversen, B. B. *J. Am. Chem. Soc.* **2003**, *125*, 11088.
- Poulsen, R. D.; Bontien, A.; Graber, T.; Iversen, B. B. *Acta Crystallogr., Sect. A* **2004**, *60*, 382.
- Poulsen, R. D.; Bontien, A.; Chevalier, M.; Iversen, B. B. *J. Am. Chem. Soc.* **2005**, *127*, 9156.
- Clausen, H. F.; Overgaard, J.; Chen, Y. S.; Iversen, B. B. In preparation.
- Lee, J. J.; Lee, G. H.; Wang, Y. *Chem.—Eur. J.* **2002**, *8*, 1821.

- (58) Jauch, W.; Reehuis, M. *Phys. Rev. B* **2002**, 65.
- (59) Gibbs, G. V.; Downs, R. T.; Prewitt, C. T.; Rosso, K. M.; Ross, N. L.; Cox, D. F. *J. Phys. Chem. B* **2005**, 109, 21788.
- (60) Gibbs, G. V.; Cox, D. F.; Rosso, K. M.; Ross, N. L.; Downs, R. T.; Spackman, M. A. *J. Phys. Chem. B* **2007**, 111, 1923.
- (61) Pearson, R. G. *Inorg. Chem.* **1988**, 27, 734.
- (62) Mayer, B.; Uhlenbrock, S.; Neumann, M. *J. Electron Spectrosc. Relat. Phenom.* **1996**, 81, 63.
- (63) Wu, Z. Y.; Xian, D. C.; Hu, T. D.; Xie, Y. N.; Tao, Y.; Natoli, C. R.; Paris, E.; Marcelli, A. *Phys. Rev. B* **2004**, 70.
- (64) Bulgakov, N. N.; Borisov, Y. A. *Russian Chem. Bull.* **1972**, 21, 21.
- (65) Hohenberg, P.; Kohn, W. *Phys. Rev.* **1964**, 136, B864.
- (66) Abramov, Y. A. *Acta Crystallogr.* **1997**, A53, 264.
- (67) Sasaki, S.; Fujino, K.; Takeuchi, Y.; Sadanaga, R. *Acta Crystallogr., Sect. A* **1980**, 36, 904.
- (68) Oganov, A. R.; Gillan, M. J.; Price, G. D. *Phys. Rev. B (Condensed Matter Mater. Phys.)* **2005**, 71, 064104.
- (69) Gibbs, G. V. *Am. Mineral.* **1982**, 67, 421.
- (70) Hoffmann, R. *Solids and Surfaces: A Chemist's View of Bonding in Extended Structures*; VCH Publishers: New York, 1988.
- (71) Lager, G. A.; Meagher, E. P. *Am. Mineral.* **1978**, 63, 365.
- (72) Pacalo, R. E.; Graham, E. K. *Phys. Chem. Miner.* **1991**, 18, 69.
- (73) Rodehorst, U.; Geiger, C. A.; Armbruster, T. *Am. Mineral.* **2002**, 87, 542.
- (74) Francis, C. A.; Ribbe, P. H. *Am. Mineral.* **1980**, 65, 1263.
- (75) Fjellvag, H.; Gronvold, F.; Stolen, S. *J. Solid State Chem.* **1996**, 124, 52.
- (76) Folco, L.; Mellini, M. *Eur. J. Mineral.* **1997**, 9, 969.
- (77) Sueno, S.; Cameron, M.; Prewitt, C. T. *Am. Mineral.* **1976**, 61, 38.
- (78) Armbruster, T.; Geiger, C. A.; Lager, G. A. *Am. Mineral.* **1992**, 77, 512.
- (79) Taran, M. N.; Nestola, F.; Ohashi, H.; Koch-Muller, M.; Balic-Zunic, T.; Olsen, L. A. *Am. Mineral.* **2007**, 92, 1616.
- (80) Morimoto, N.; Tokonami, M.; Watanabe, M.; Koto, K. *Am. Mineral.* **1974**, 59, 475.
- (81) Kimata, M.; Nishida, N. *Neues Jahrbuch Mineral.–Monatshefte* **1987**, 160.
- (82) Wyckoff, R. W. G. *Crystal Structures*, 2nd ed.; Interscience Publishers: New York, 1963.

JP804280J